

Northumbria Research Link

Citation: Guo, Yan, Liu, Hu, Wang, Dedong, El-Bahy, Zeinhom M., Althakafy, Jalal T., Abo-Dief, Hala M., Guo, Zhanhu, Xu, Bin, Liu, Chuntai and Shen, Changyu (2022) Engineering hierarchical heterostructure material based on metal-organic frameworks and cotton fiber for high-efficient microwave absorber. *Nano Research*, 15 (8). pp. 6841-6850. ISSN 1998-0124

Published by: Springer

URL: <https://doi.org/10.1007/s12274-022-4533-x> <<https://doi.org/10.1007/s12274-022-4533-x>>

This version was downloaded from Northumbria Research Link: <https://nrl.northumbria.ac.uk/id/eprint/49291/>

Northumbria University has developed Northumbria Research Link (NRL) to enable users to access the University's research output. Copyright © and moral rights for items on NRL are retained by the individual author(s) and/or other copyright owners. Single copies of full items can be reproduced, displayed or performed, and given to third parties in any format or medium for personal research or study, educational, or not-for-profit purposes without prior permission or charge, provided the authors, title and full bibliographic details are given, as well as a hyperlink and/or URL to the original metadata page. The content must not be changed in any way. Full items must not be sold commercially in any format or medium without formal permission of the copyright holder. The full policy is available online: <http://nrl.northumbria.ac.uk/policies.html>

This document may differ from the final, published version of the research and has been made available online in accordance with publisher policies. To read and/or cite from the published version of the research, please visit the publisher's website (a subscription may be required.)

Engineering Hierarchical Heterostructure Material Based on Metal-Organic Frameworks and Cotton Fiber for High-Efficient Microwave Absorber

Yan Guo,¹ Hu Liu,^{1*}, Dedong Wang,¹ Zeinhom M. El-Bahy,² Jalal T. Althakafy,³
Hala M. Abo-Dief,⁴ Zhanhu Guo,^{5*} Ben Bin Xu,⁶ Chuntai Liu,¹ Changyu Shen¹

¹Key Laboratory of Materials Processing and Mold (Zhengzhou University), Ministry of Education; National Engineering Research Center for Advanced Polymer Processing Technology, Zhengzhou University, Zhengzhou, Henan 450002 China

²Department of Chemistry, Faculty of Science, Al-Azhar University, Nasr City 11884, Cairo, Egypt

³Chemistry Department, Faculty of Applied Science, Umm Al-Qura University, Makkah, Saudi Arabia

⁴Department of Chemistry, College of Science, Taif University, P.O. Box 11099 Taif 21944, Saudi Arabia

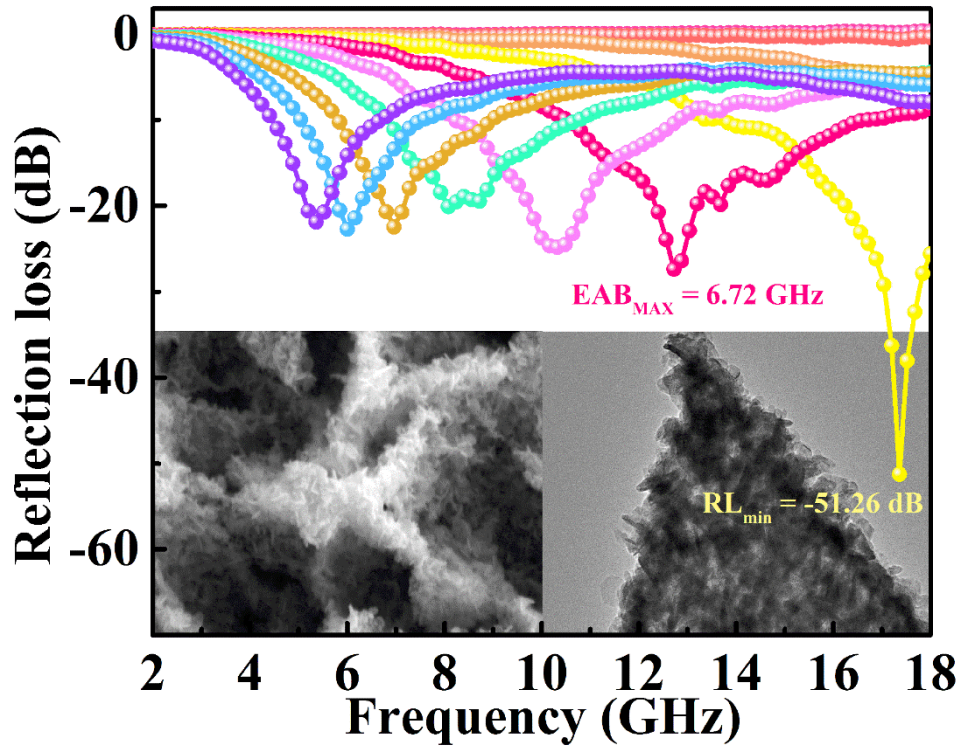
⁵Integrated Composites Laboratory (ICL), Department of Chemical & Biomolecular Engineering, University of Tennessee, Knoxville, TN 37996 USA

⁶Department of Mechanical and Construction Engineering, Faculty of Engineering and Environment, Northumbria University, Newcastle upon Tyne, NE1 8ST, UK

**: Correspondence authors*

E-mail addresses: liuhu@zzu.edu.cn (H. L.); zguo10@utk.edu (Z. G.)

Graphical Table of Contents



Hierarchical heterostructure WS_2/CoS_2 @carbonized cotton fiber (CCF) derived from metal-organic frameworks (MOFs) anchored cotton fiber possesses multiple loss mechanisms and exhibits high-performance electromagnetic wave absorption capacity.

ABSTRACT: Rational construction of hierarchical multi-component materials with abundant heterostructure is evolving as a promising strategy to achieve excellent metal-organic frameworks (MOFs) based electromagnetic wave (EMW) absorbers. Herein, hierarchical heterostructure WS_2/CoS_2 @carbonized cotton fiber (CCF) was fabricated using the ZIF-67 MOFs nanosheets anchored cotton fiber (ZIF-67@CF) as a precursor through the tungsten etching, sulfurization, and carbonization process. Apart from the synergetic effect of dielectric-magnetic dual-loss mechanism, the hierarchical heterostructure and multicomponent of WS_2/CoS_2 @CCF also display improved impedance matching. Furthermore, numerous W-S-Co band and heterojunction interfaces of heterogeneous WS_2/CoS_2 is beneficial to promoting additional interfacial/dipole polarization loss and conductive loss, thereby enhancing the EMW attenuation performance. Based on the percolation theory, a good balance between impedance matching and EMW absorption capacity was achieved for the WS_2/CoS_2 @CCF/paraffin composite with 20 wt% filler loading, exhibiting strong EMW absorption capability with a minimum reflection loss (RL_{\min}) value of -51.26 dB at 17.36 GHz with 2 mm thickness and a maximum effective absorption bandwidth (EAB_{\max}) as wide as 6.72 GHz. Our research will provide new guidance for designing high-efficient MOFs derived EMW absorbers.

KEYWORDS: hierarchical, heterostructure, sulfurization, metal-organic framework, microwave absorber

1 Introduction

With the advent of 5G information age, electromagnetic interference (EMI) and radiation produced by electronic communication devices have become a serious issue in human health, electronic information safety and device performance [1-6]. Thus, it is urgent to explore low-cost and high-efficient electromagnetic microwave wave (EMW) absorbers, which could effectively attenuate the incident EMW by transforming them into heat or other forms of energy. Normally, ideal EMW absorbing materials should possess the essential characteristics of thin matching thickness, broad bandwidth, strong absorption, and light weight [5-9]. To meet the above requirements, reasonable structure and component design has drawn considerable attention in advanced EMW absorbers.

Nowadays, carbon materials including carbon nanotubes [10], graphene [11] and carbon aerogels [12] have been widely used in the field of EMW absorption due to their high dielectric loss, low density and good environmental stability. Nevertheless, the complex synthesis process and high cost of them have seriously hindered their large-scale applications. Owing to the merits of sustainability, low-cost, nontoxicity and facile process, the pyrolysis products of biomass materials such as platanus [13], wood [14], cattail [15] and lotus leaf [16] have been widely considered as the new carbon based EMW absorbing materials. More importantly, their special intrinsic structure (e.g., cellular structure, hierarchical structure, interwoven network structure and hollow tube-like structure) and amounts of defects and residual functional groups are also helpful for extending transmission path through multiple reflections and generating enhanced polarization loss, exhibiting superior EMW absorption performance. However, the high conductivity of carbon

materials can also usually bring serious impedance mismatching that lead to unexpected reflection of incident EMW.

Generally, optimized impedance matching could be effectively achieved through engineering magnetic/dielectric multicomponent materials with rational structure design. In addition, the dielectric and magnetic dual-loss mechanism is also beneficial for improved loss capacity simultaneously. With the rapid development of metal organic frameworks (MOFs) materials, carbon/metal composites prepared from calcinated MOFs present great application potential in EMW absorption because of their merits of high porosity, controllable structure, and adjustable composition. Meanwhile, MOFs modified fiber and fabric have also been widely investigated and used as a precursor for carbonization, which could effectively avoid the discontinuity and aggregation of single calcinated MOFs particles, constructing high-efficient electromagnetic attenuation network easily. What's more, amounts of heterogeneous interfaces can also be simultaneously constructed to contribute additional interfacial polarization loss, boosting the EMW absorption capability. For example, Wang et al. used cotton fiber (CF) and Co-ZIF as precursors to fabricate the heterostructure Co/CNTs-MXene@CF through the self-assembly and thermocatalytic technology, achieving a minimum reflection loss (RL_{\min}) of -61.41 dB at 2.52 mm and a broad maximum effective absorption bandwidth (EAB_{\max}) of 5.04 GHz [17]. Xu et al. synthesized CC/ZIFs with abundant heterogeneous interface and defects derived from CoZn-ZIF and cotton fiber cloth, showing a RL_{\min} of -36.0 dB and EAB_{\max} up to 11.6 GHz [18].

In this study, hierarchical heterostructure WS_2/CoS_2 @carbonized cotton fiber (CCF) was fabricated using the ZIF-67 nanosheets anchored cotton fiber (ZIF-67@CF) as a precursor through

the tungsten etching, sulfurization, and carbonization process. Apart from the synergistic dielectric-magnetic dual-loss mechanism, the special hierarchical structure and multicomponent of $\text{WS}_2/\text{CoS}_2@\text{CCF}$ also facilitate an improvement in the impedance matching. Importantly, the amounts of heterogeneous WS_2/CoS_2 is also beneficial for additional interfacial/dipole polarization loss and conduction loss, resulting in enhanced EMW attenuation. As a result, the prepared $\text{WS}_2/\text{CoS}_2@\text{CCF}$ shows a superior EMW absorption capacity with an RL_{min} value of -51.26 dB at 2 mm and a wide EAB_{max} of 6.72 GHz under the filler loading of 20 wt%. This work will undoubtedly provide a new strategy for engineering high-efficient MOFs derived EMW absorbers.

2 Experimental sections

2.1 Materials and chemicals

Pure cotton face towel (Huizhou Jianrou Industrial Co., Ltd.) was bought from supermarket and served as the biomass carbon resource. 2-Methylimidazole was purchased from Shanghai Macklin Biochemical Co., Ltd. $\text{Co}(\text{NO}_3)_2 \cdot 6\text{H}_2\text{O}$ and Na_2WO_4 were supplied by Tianjin Kemiou Chemical Reagent Co., Ltd. Thiourea was provided by Sinopharm Chemical Reagent Co., Ltd. All the materials and chemicals were used as received without further purification.

2.2 Preparation procedure

Synthesis of ZIF-67@CF: According to our previous work, ZIF-67 precursor solution was first prepared by dissolving 0.58 g of $\text{Co}(\text{NO}_3)_2 \cdot 6\text{H}_2\text{O}$ and 1.31 g of 2-methylimidazole into 40 mL deionized (DI) water under vigorous magnetic stirring for 10 min. Then, a piece of cotton face towel ($4 \times 4 \text{ cm}^2$) was vertically immersed into the obtained purple ZIF-67 precursor solution for

4 h at 25 °C to grow ZIF-67 onto the cotton fiber (CF) surface, followed by washing with DI water and ethanol, and drying at 40 °C overnight, obtaining the purple ZIF-67@CF.

Preparation of WS₂/CoS₂@CCF: 0.2 g Na₂WO₄ was dissolved thoroughly in 20 mL DI water and uniformly mixed with 80 mL ethanol, and the obtained ZIF-67@CF was then immersed into the mixed solution at 85 °C until the purple color disappeared completely. After being rinsed with DI water and ethanol and dried at 40 °C, it was placed in the center of tube furnace with 1 g of sulfur powder at the upstream and calcinated at 500 °C in N₂ atmosphere (30 mL min⁻¹) for 2 h with a heating rate of 5 °C/min, obtaining the designed WS₂/CoS₂@CCF heterostructure material. For comparison, CCF and CoS₂@CCF were also prepared by calcinating the CF and ZIF-67@CF directly under the same condition, respectively.

2.3 Characterizations

Micromorphology and structure of the as-prepared materials were observed by transmission electron microscope (TEM, JEOL JEM-2010) and field emission scanning electron microscope (FESEM, JEOL JSM-7500F). The lattice structure of material was analyzed by X-ray diffraction (XRD, Bruker, D8 advance) in the range of 10-80° using Cu tube ($\lambda = 1.5418 \text{ \AA}$, 10°/min). X-ray photoelectron spectroscopy (XPS, ESCALAB 250 XI) was used to investigate the surface electronic property of materials. A certain amount of the prepared WS₂/CoS₂@CCF was used as a filler to mix with paraffin and pressed into coaxial ring (thickness = 3 mm, $\Phi_{\text{outer}} = 7.00 \text{ mm}$, $\Phi_{\text{inner}} = 3.04 \text{ mm}$), and the electromagnetic parameters were measured using the Keysight N5222B vector network analyzer in the frequency range of 2-18 GHz. In this study, series of

coaxial rings with different $\text{WS}_2/\text{CoS}_2@\text{CCF}$ loading (10, 15, 20, 25 and 30 wt%) was prepared to study the effect of filler loading on EMW absorption performances.

3 Results and discussion

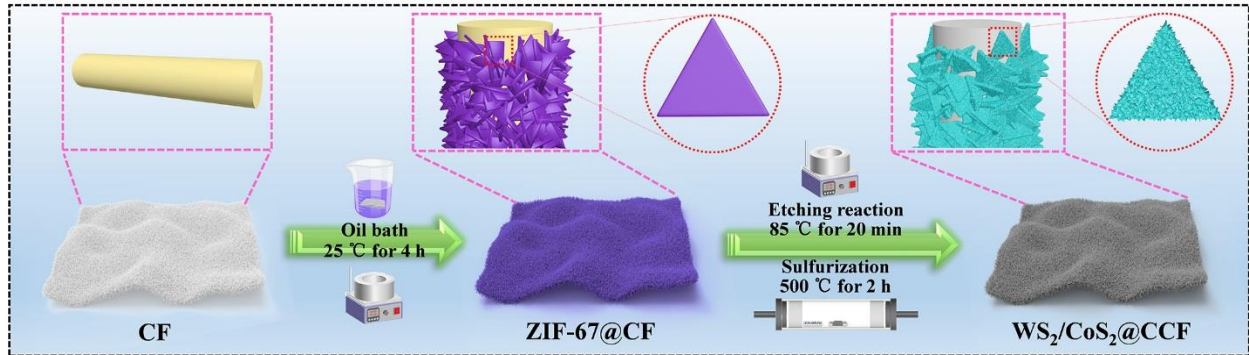


Figure 1. Schematic diagram of the preparation process of $\text{WS}_2/\text{CoS}_2@\text{CCF}$.

Figure 1 shows the preparation procedure of the designed $\text{WS}_2/\text{CoS}_2@\text{CCF}$, including the in-situ growth of ZIF-76, tungsten etching, sulfurization and carbonization. Firstly, amounts of functional groups (-OH, -O-) of CF enable it to be well wetted in the ZIF-67 precursor solution and serve as active sites to absorb Co^{2+} ions, which reacts with the organic linker of 2-methylimidazole to form the homogeneous anchored ZIF-67 on the whole fiber surface, and the CF color also changes from white to purple (Figure S1a&b). Then, Na_2WO_4 solution was applied to etch the generated ZIF-67, resulting in the collapse of MOF framework and the introduction of heterogeneous W atom. Finally, high temperature sulfurization process was conducted, during which thiourea was used as a sulfur source to react with Co and W atoms to form metal sulfides, and the formed W-S-Co bond enable the existence of abundant heterojunction for the final product. Meanwhile, the CF and MOF framework were also carbonized at the same time, obtaining the designed black $\text{WS}_2/\text{CoS}_2@\text{CCF}$ (Figure S1c). Here, it should be noted that the low-

electronegativity sulfur in heterogeneous WS_2/CoS_2 can effectively accelerate the transfer of electrons, endowing the $\text{WS}_2/\text{CoS}_2@\text{CCF}$ with improved conductivity.

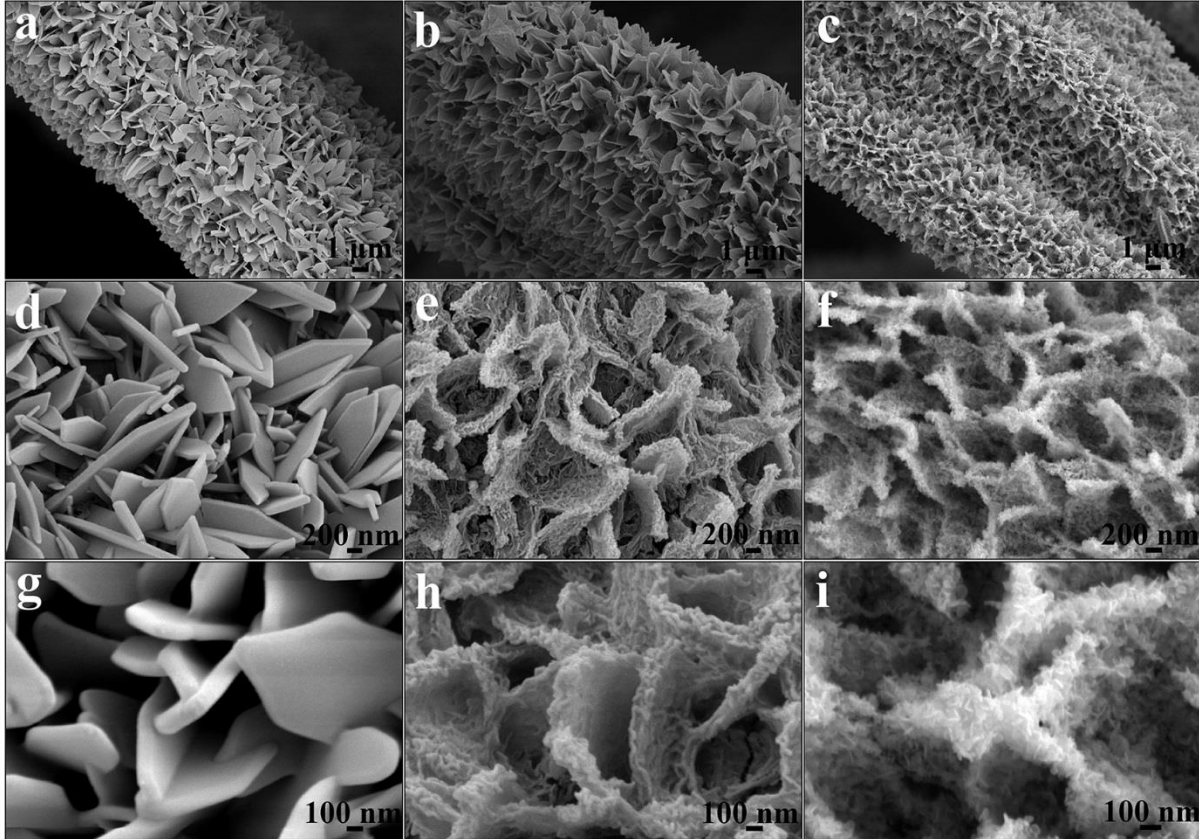


Figure 2. SEM images of (a, d & g) ZIF-67@CF, (b, e & h) Na_2WO_4 etched ZIF-67@CF, and (c, f & i) $\text{WS}_2/\text{CoS}_2@\text{CCF}$ with different magnifications.

Micromorphology and structure evolution during the preparation process was further investigated. Specifically, as shown in [Figure S2](#), the pristine CF displays an average diameter of about 10-15 μm and a special wrinkled surface, which is beneficial for immobilizing nanoparticles. As for the ZIF-67@CF ([Figure 2a,d&g](#)), the in-situ growth of triangular ZIF-67 nanosheets with smooth surface and a thickness of about 150 nm are cross vertically aligned on the whole fiber surface, constructing many pores with the magnitude of micrometers. After etching with Na_2WO_4 solution, the basic morphology structure of ZIF-67 is well maintained ([Figure 2b](#)), but the smooth

surface turns to be wrinkled with lots of obvious ridges (Figure 2e&h), which can be ascribed to the collapse of MOF framework. For WS₂/CoS₂@CCF, smaller and denser arranged nanosheets are clearly observed (Figure 2c) because of the shrinkage of CF and MOF framework after the high temperature pyrolysis treatment. From the magnification images in Figure 2f&i, it can be observed that the triangular nanosheet turns to be rougher and looser, whose subunits are assembled by tightly stacked nanoflakes with numerous nano-sized pores. Compared with the surface of CoS₂@CCF anchored with amounts of nanoparticles (Figure S3), the unique hierarchical porous structure is beneficial for optimizing the impedance matching and accelerating the multiple reflection of incident EMW, achieving the improved EMW absorption capacity. In addition, the cross connected carbonized triangular nanosheets and the tightly stacked conductive WS₂/CoS₂ nanoflakes can also accelerate electron transfer to increase the conduction loss effect.

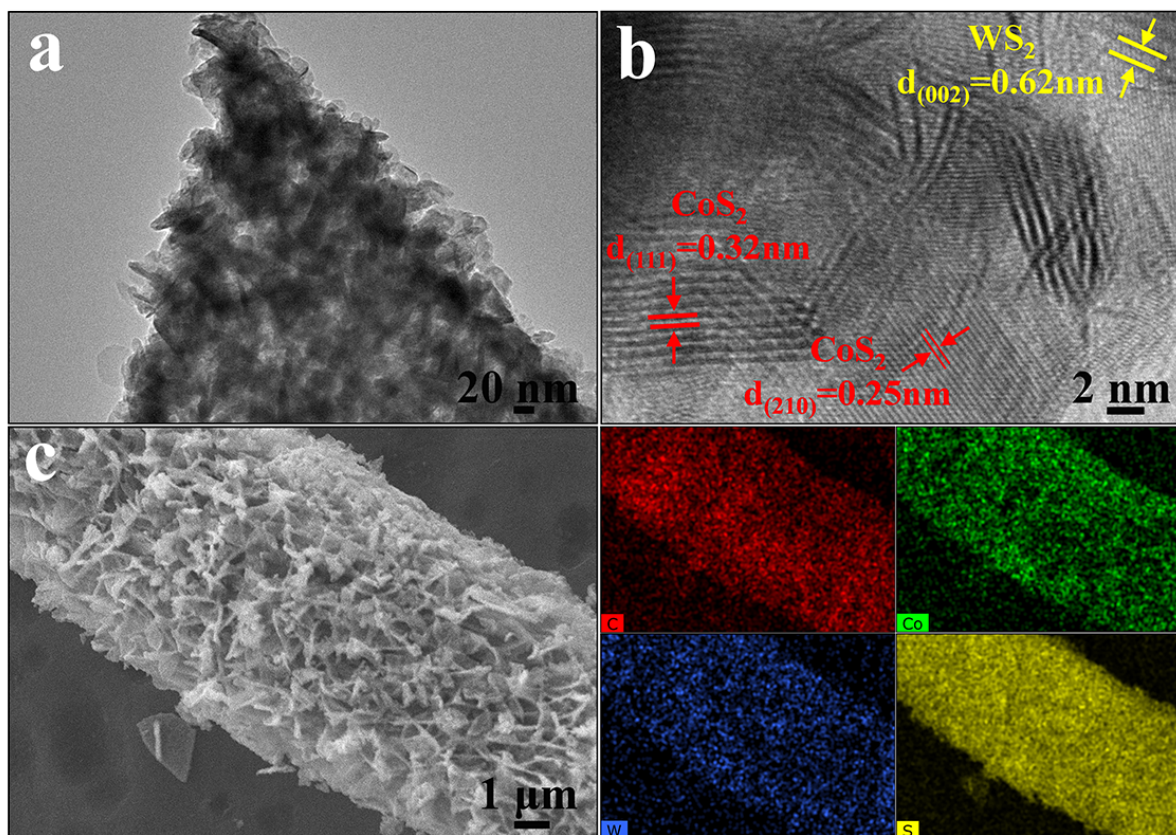


Figure 3. (a) TEM image and (b) HRTEM image of WS₂/CoS₂. (c) Elemental mappings images of C, Co, W and S of WS₂/CoS₂@CCF.

More detail structure information of WS₂/CoS₂@CCF was further investigated. As shown in [Figure 3a](#), it can be clearly seen from the TEM image that the triangular nanosheet contains numerous nanoflakes, which is in good agreement with the SEM images. From the HRTEM image of the nanoflake in [Figure 3b](#), we can see a visible parallel lattice fringe with an interplanar distance of 0.62 nm, which can be indexed to the (002) crystal plane of WS₂, while the lattice spacing of 0.32 and 0.25 nm correspond to the (111) and (210) crystal plane of CoS₂ [19]. Notably, the long-range continuous interfaces between CoS₂ and WS₂ can be clearly observed, and the intermediate S atoms act as bridge to connect W and Co, providing multiple electron transfer paths. Energy dispersive X-ray spectrometer (EDS) mapping of WS₂/CoS₂@CCF was also conducted ([Figure](#)

S4). As illustrated in Figure 3c, the elements of C, N, Co, W and S are homogeneously distributed on the whole fiber surface, further demonstrating the successful fabrication of WS₂/CoS₂@CCF. Therefore, the hierarchical porous structure, abundant heterojunction interfaces, conductive carbonaceous component, and heteroatom doping of WS₂/CoS₂@CCF will undoubtedly endow it with great potential for EMW absorption application.

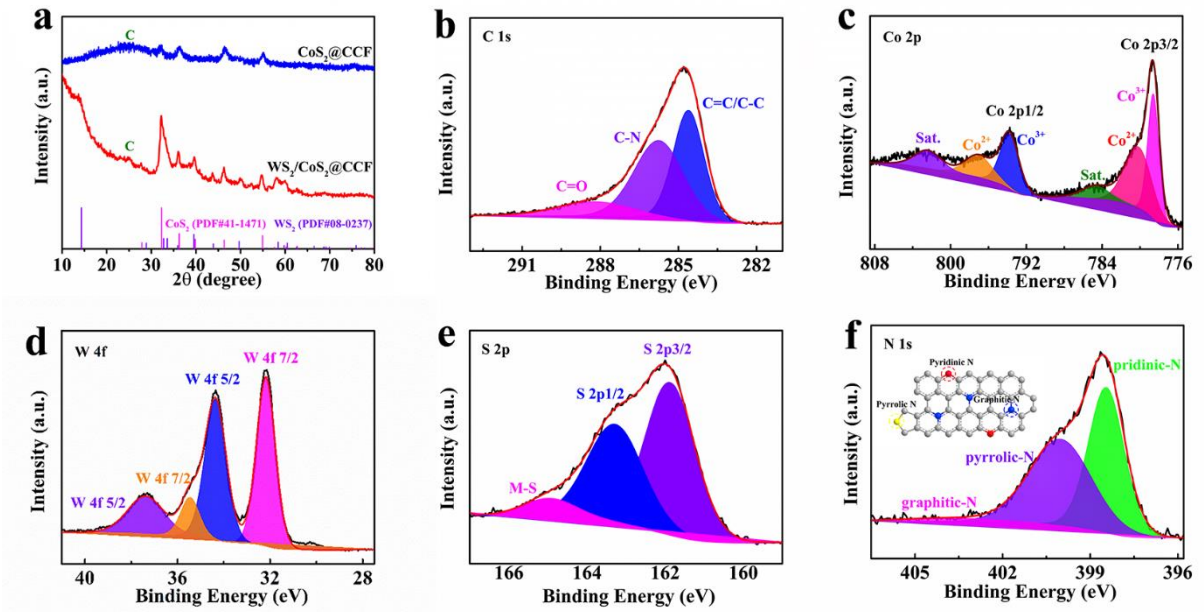


Figure 4. (a) XRD patterns of CoS₂@CCF and WS₂/CoS₂@CCF. XPS spectra of (a) C 1s, (b) Co 2p, (d) W 4f, (e) S 2p and (f) N 1s for WS₂/CoS₂@CCF. The insert in (f) is the schematic structure of N-doped carbon with graphitic N, pyrrolic N, and pyridinic N.

To analyze the phase information and crystal structure of CoS₂@CCF and WS₂/CoS₂@CCF, XRD patterns of them were performed and illustrated in Figure 4a. The broad diffraction peaks at about 25° for the two samples can be assigned to the (002) plane of graphite carbon derived from the pyrolyzed CF and MOF skeleton. For CoS₂@CCF, the obvious representative diffraction peaks at 32.3°, 36.0°, 46.3° and 54.7° correspond to the (200), (210), (220) and (311) crystal planes of CoS₂ (JCPDS card: 41-1471) [19], respectively. From the pattern of WS₂/CoS₂@CCF, apart from

the typical diffraction peaks of CoS₂, the others at 14.4°, 43.7° and 58.0° are indexed to the (002), (104), (110) planes of WS₂ (JCPDS card: 08-0237) [20], respectively. All these results suggest that WS₂ and CoS₂ has been successfully prepared and incorporated into the designed high temperature sulfurization product of WS₂/CoS₂@CCF.

Surface chemical composition and valence states of WS₂/CoS₂@CCF were further analyzed via X-ray photoelectron spectroscopy (XPS). From the XPS full-survey-scan spectrum shown in [Figure S5](#), it can be confirmed that the main elements of WS₂/CoS₂@CCF are Co, O, N, C, S and W, which are coincided with the EDS results. Specifically, the high resolution C 1s spectrum can be split into three peaks at 284.8 eV, 285.7 eV and 288.2 eV, which are corresponded to the C=C/C-C, C-N and C=O groups ([Figure 4b](#)) [21], respectively. In general, all these carbon bonds are beneficial for fast electron transfer to achieve good conductivity. For the Co 2p spectrum ([Figure 4c](#)), the peaks at 778.6 eV and 793.8 eV are assigned to the Co 2p_{3/2} and Co 2p_{1/2} of Co³⁺, respectively. The peaks at 780.3 eV and 797.2 eV are ascribed to the presence of Co²⁺ valence state, while there are also two satellite peaks at 784.8 eV and 802.5 eV [10, 22]. [Figure 4d](#) displays the deconvoluted W 4f spectrum, where the first pair of peaks at about 32.2 eV and 34.3 eV belong to W 4f_{7/2} and W 4f_{5/2} of W⁴⁺, and two peaks (35.4 eV and 37.4 eV) in the other pair to W⁶⁺ of WO₃ are also observed because of the oxidation [20, 23]. As presented in [Figure 4e](#), the S 2p spectrum clearly exhibits the two major peaks of S 2p_{3/2} and S 2p_{1/2} at about 161.9 eV and 163.3 eV. And the peak at 164.9 eV stands for the typical metal-sulfur (M-S) bond in the material [22]. The N 1s spectrum in [Figure 4f](#) displays the peaks 398.5 eV, 400.1 eV and 402.0 eV, which are related to pyridinic N, pyrrolic N and graphitic N, indicating the successful N-doping in carbon matrix [24].

Here, the electronegative N atoms act as polarization center under alternating electromagnetic field to contribute dipolar relaxation loss, and the N atom can also improve the electron transport capacity through providing electron to pair with the conjugate ring, generating the conduction loss [25].

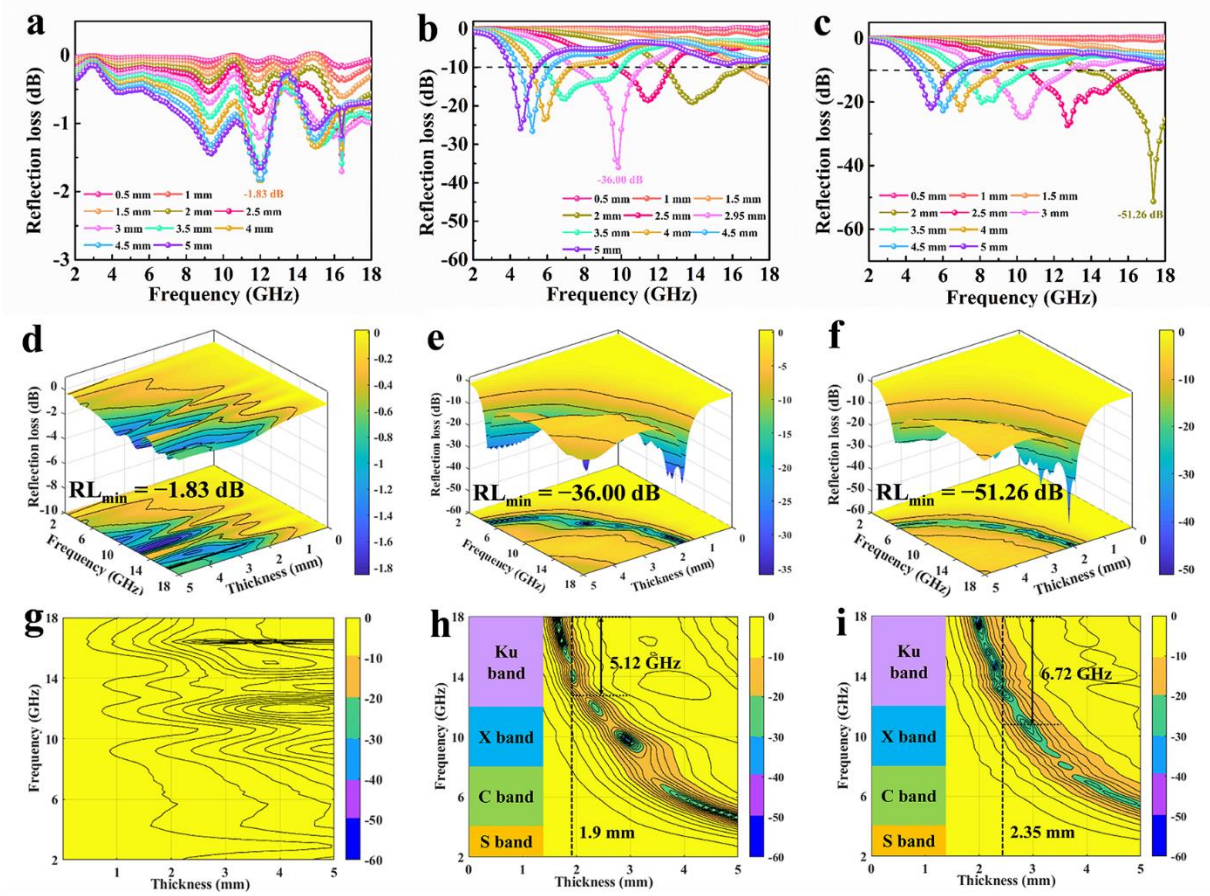


Figure 5. RL curves and the corresponding 3D and 2D contour plots of (a, d & g) CCF, (b, e & h) CoS₂@CCF and (c, f & i) WS₂/CoS₂@CCF.

According to transmission line theory, EMW absorption capacity is usually evaluated by reflection loss (RL), which can be calculated using the following equations: [12]

$$RL(\text{dB}) = 20 \log \left| \frac{(Z_{in} - Z_0)}{(Z_{in} + Z_0)} \right| \quad (1)$$

$$Z_{in} = Z_0 \sqrt{\frac{\mu_r}{\epsilon_r}} \tanh \left[j(2\pi f d / c) \sqrt{\mu_r \epsilon_r} \right] \quad (2)$$

where Z_{in} is the normalized input impedance of the absorber, Z_0 refers to the impedance of free space, f is the frequency of EMW, d and c represent the absorber thickness and the velocity of the microwave in free space, ϵ_r and μ_r are the complex permittivity and permeability. General speaking, the frequency range in which the RL value is smaller than -10 dB (90% attenuation of incident EM energy) is called the effective absorption bandwidth (EAB). The RL curves, and the corresponding 3D and 2D contour plots of CCF, CoS₂@CCF and WS₂/CoS₂@CCF with a filler loading of 20 wt% in the range of 2-18 GHz are displayed in Figure 5. As shown in Figure 5a, d&g, CCF displays a RL_{min} value of only -1.83 dB at 11.92 GHz with a thickness of 4.00 mm and no available EAB, which cannot satisfy the basic engineering requirement of -10 dB. As for the CoS₂@CCF (Figure 5b, e&h), the RL_{min} value increases to -36.00 dB at 9.84 GHz with a thickness of 2.95 mm and the EAB_{max} covers 5.12 GHz from 12.88 to 18 GHz at 1.9 mm. As expected, the WS₂/CoS₂@CCF exhibits the strongest EMW absorption capacity with an RL_{min} value of -51.26 dB at 17.36 GHz and 2 mm thickness (Figure 5c, f&i), demonstrating that about 99.999% EMW can be consumed efficiently. Meanwhile, a broader EAB_{max} of 6.72 GHz (11.28-18 GHz) can also be achieved for the sample with 2.35 mm thickness, covering all the Ku band and part of X band. Hence, it can be inferred that the hierarchical porous structure and amounts of heterojunction interfaces can significantly affect the EMW absorbing performance of the absorbers.

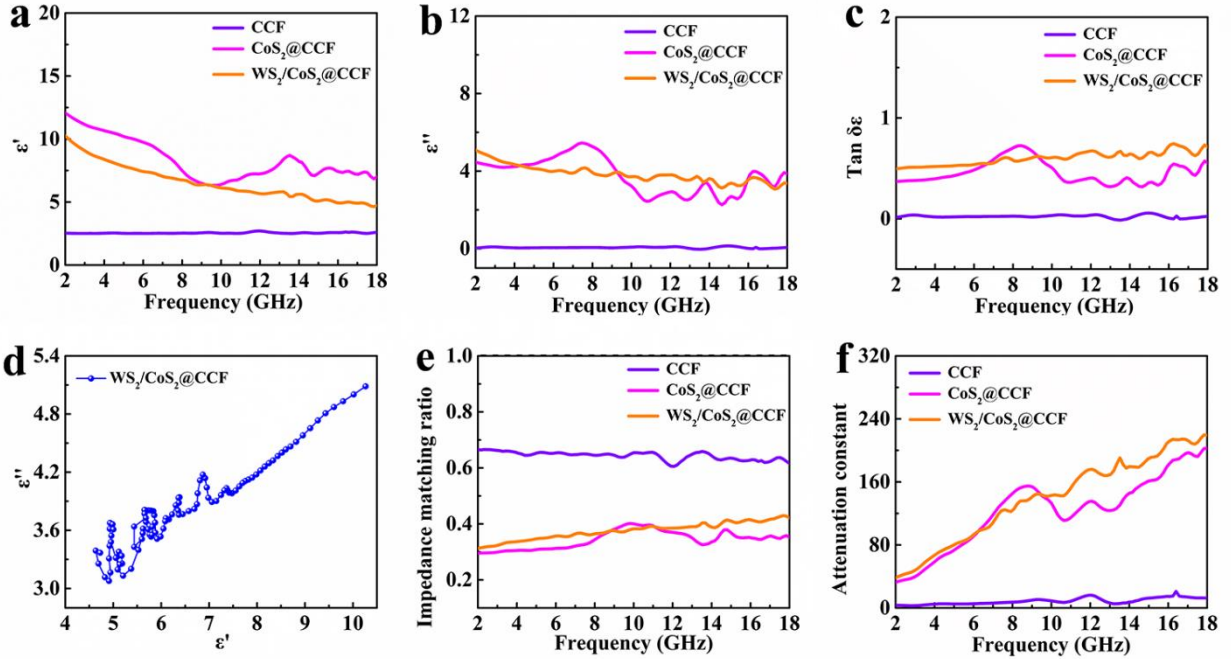


Figure 6. (a) Real permittivity (ϵ'), (b) imaginary permittivity (ϵ''), (c) dielectric loss tangents, (d) Cole-Cole curve, (e) impedance matching ratio and (f) attenuation constant of CCF, CoS₂@CCF and WS₂/CoS₂@CCF.

As is well-known, EMW absorption performances of sample are closely related to the corresponding electromagnetic parameters of complex permittivity ($\epsilon_r = \epsilon' - j\epsilon''$) and complex permeability ($\mu_r = \mu' - j\mu''$). The real part (ϵ' and μ') represents the electrical and magnetic energy storage capability, while the imaginary part (ϵ'' and μ'') stands for the electrical and magnetic energy dissipation ability. Besides, dielectric loss tangent ($\tan \delta_\epsilon = \epsilon''/\epsilon'$) and magnetic loss tangent ($\tan \delta_\mu = \mu''/\mu'$) were also calculated to evaluate the dielectric and magnetic dissipation ability [11]. Figure 6 displays that the electromagnetic parameters of CCF, CoS₂@CCF and WS₂/CoS₂@CCF with a 20 wt% filler loading in the frequency range of 2-18 GHz tested by the coaxial method. Obviously, as presented in Figure 6a&b, both the ϵ' and ϵ'' values of them show a continuous downward trend with increasing frequency, revealing a typical frequency dispersion phenomenon due to the delayed charge transfer and polarization response associated with the changing electrical

field [26-28]. In addition, both the ϵ' and ϵ'' values of CoS₂@CCF are much higher than those of CCF, but the ϵ' and ϵ'' values of WS₂/CoS₂@CCF is slightly lower and higher than that of CoS₂@CCF, respectively, demonstrating that the introduction of hierarchical heterostructure could further tune the permittivity to achieve better impedance matching. What's more, obvious relaxation peaks are clearly observed for the ϵ'' curves of CoS₂@CCF and WS₂/CoS₂@CCF, indicating the existence of polarization-relaxation process. In general, these peaks at low and high frequency range are mainly caused by dipole polarization and interface polarization, which are beneficial for the improved dielectric loss. Furthermore, as shown in [Figure 6c](#), the WS₂/CoS₂@CCF exhibits the highest value in the whole testing frequency range, demonstrating the strongest dielectric loss capacity.

In general, conduction loss and polarization loss contribute to the dielectric loss. Compared with CCF and CoS₂@CCF, the hierarchical heterostructure of WS₂/CoS₂@CCF mainly supplies connected 3D porous conductive network and heterojunction interfaces to increase the conduction loss and interfacial polarization loss. Here, Debye theory was used to analyze the polarization loss mechanism according to the following formula: [11]

$$\left(\epsilon' - \frac{\epsilon_s + \epsilon_\infty}{2}\right)^2 + (\epsilon'')^2 = \left(\frac{\epsilon_s - \epsilon_\infty}{2}\right)^2 \quad (6)$$

where the ϵ_s and ϵ_∞ stands for the static permittivity and relative dielectric permittivity under high frequency limit, respectively. In general, a semicircle (Cole–Cole semicircle) in the obtained ϵ' - ϵ'' curve represents a dielectric polarization relaxation process [29]. However, it always delineates nonstandard semicircle and linear tail due to the conductivity of absorber, and a longer tail indicates

stronger conduction loss. As presented in [Figure 6d&S6](#), obvious multiple nonstandard Cole–Cole semicircles are observed for all samples, indicating the existence of polarization relaxation processes. Specifically, the residual oxygen containing functional groups and defects in CCF act as the dipole active sites to generate the dipole polarization loss, but additional interfacial polarization loss arising from the accumulated electrons at the CCF-CoS₂ interfaces under the applied electrical field and dipole polarization loss from the doped N elements are produced for CoS₂@CCF. As for WS₂/CoS₂@CCF, high temperature sulfurization introduced S element and heterojunction interfaces of WS₂/CoS₂ contribute stronger dipole/interfacial polarization loss. Furthermore, the linear tail which represents the existence of conduction loss is clearly observed for CoS₂@CCF and WS₂/CoS₂@CCF, but the WS₂/CoS₂@CCF displays a much longer tail, which can be ascribed to the low-electronegativity sulfur in heterogeneous WS₂/CoS₂ that can effectively accelerate the transfer of electrons, supplying more effective conduction loss.

Moreover, as shown in [Figure S7a&b](#), the value of μ' and μ'' fluctuates around 1 and 0, respectively, indicating a weak magnetic behavior. Besides, it can be observed that the μ'' and $\tan \delta_\mu$ of WS₂/CoS₂@CCF and of CoS₂@CCF exhibit a similar trend with several resonance peaks in the curves, illustrating the presence of magnetic loss. As displayed in [Figure S8](#), the eddy current coefficient C_0 ($C_0 = \mu''(\mu')^{-2} f^{-1} = 2\pi\mu_0 d^2 \sigma / 3$) [30] of CoS₂@CCF and WS₂/CoS₂@CCF fluctuates within the testing frequency range and tends to be horizontal in the range of 9~13 GHz, confirming that magnetic loss is caused by eddy current, natural resonance and exchange resonance simultaneously [31, 32]. Importantly, the $\tan \delta_\mu$ value in [Figure S7c](#) is much lower than the $\tan \delta_\epsilon$ value, indicating the dielectric loss dominant EMW attenuation mechanism.

General speaking, impedance matching ratio (Z) and attenuation constant (α) are the two key factors to affect the EMW absorption capacity of materials. Impedance matching ratio is closely related to the ability of incident EMW to enter the interior of absorbers, and a Z value close to 1 means that almost all the EMW can penetrate the absorbers without being reflected, showing an ideal impedance matching. The Z values of CCF, CoS₂@CCF and WS₂/CoS₂@CCF were calculated according to the following equation: [10, 33]

$$Z = \sqrt{\sqrt{(\mu''^2 + \mu'^2)} / \sqrt{(\varepsilon''^2 + \varepsilon'^2)}} \quad (4)$$

As illustrated in [Figure 6e](#), the Z value of CCF is closest to 1 among all samples, showing the best impedance matching. But the Z values of WS₂/CoS₂@CCF and CoS₂@CCF are much lower than CCF, demonstrating the worse impedance matching due to their increased conductivity according to the ε' - ε'' curves. However, WS₂/CoS₂@CCF with higher conductivity displays a better impedance matching than that of CoS₂@CCF, which can be attributed to the special hierarchical porous structure that is beneficial for the improved impedance matching. Furthermore, attenuation constant (α) was also evaluated to analyze the attention capacity through the following equation: [34, 35]

$$\alpha = \frac{\pi f \sqrt{2}}{c} \times \sqrt{(\mu'' \varepsilon'' - \mu' \varepsilon') + \sqrt{(\mu'' \varepsilon'' - \mu' \varepsilon')^2 + (\mu'' \varepsilon'' + \mu' \varepsilon')^2}} \quad (5)$$

Obviously, as shown in [Figure 6f](#), the α values of WS₂/CoS₂@CCF and CoS₂@CCF are much higher than CCF, and WS₂/CoS₂@CCF displays the highest value. Hence, WS₂/CoS₂@CCF possesses the strongest EMW attenuation capacity due to its special hierarchical porous structure and amounts of heterojunctions. As a result, appropriate impedance matching and strong EMW

attenuation capacity endow WS₂/CoS₂@CCF with excellent EMW absorption performance compared with other two samples.

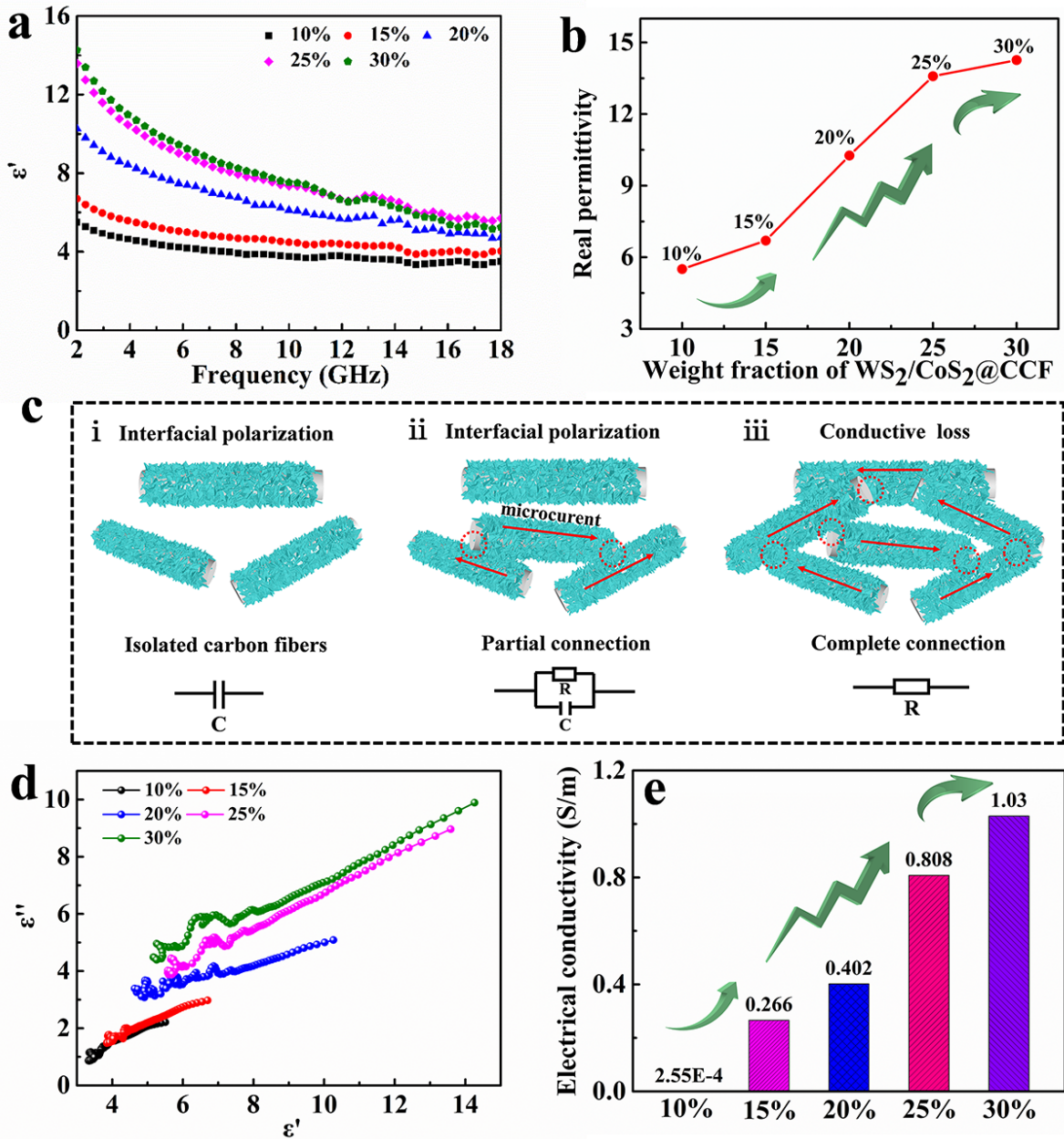


Figure 7. (a) ϵ' of paraffin composites with different WS₂/CoS₂@CCF loading in the frequency range of 2-18 GHz. (b) ϵ' of paraffin composites at 2 GHz as a function of WS₂/CoS₂@CCF loading. (c) Schematic diagram displaying the formation of the conductive network in paraffin composites. (d) Cole-Cole curves and (e) conductivity of paraffin composites with different WS₂/CoS₂@CCF loading.

Furthermore, series of paraffin composites with different WS₂/CoS₂@CCF loading was also

prepared to investigate their EMW absorption performance. As displayed in [Figure S9](#), the paraffin composites with 10 wt% WS₂/CoS₂@CCF is provided with an RL_{min} value of -17.52 dB, which is slightly decreased to -19.86 dB for a 15 wt% loading. Then, it exhibits a significant decrease to -51.26 dB for 20 wt% loading, showing a great improvement in EMW absorption. But an obvious degraded absorption is observed with further increasing the WS₂/CoS₂@CCF loading, and an RL_{min} value of -17.83 dB and -15.46 dB is obtained for 25 wt% and 30 wt % loading. Besides, the statical EAB_{max} values are 3.04 GHz, 5.92 GHz, 6.72 GHz, 6.4 GHz and 6.24 GHz for 10 wt%, 15 wt%, 20 wt%, 25 wt% and 30 wt% loading, respectively. For the dielectric loss dominant absorber, the permittivity of paraffin composites with different WS₂/CoS₂@CCF loading were further analyzed to explain the typical filler loading dependent EMW absorption performance. As displayed in [Figure 7a&S10a](#), both ϵ' and ϵ'' increase with increasing WS₂/CoS₂@CCF loading in the frequency range of 2-18 GHz, and the ϵ' and ϵ'' value at 2 GHz as a function of the WS₂/CoS₂@CCF loading display a typical percolation behavior ([Figure 7b&S10b](#)) [29]. Specifically, the value of ϵ' and ϵ'' shows a subtle increase from 5.5 to 6.7 and 2.2 to 3.0 for the lower WS₂/CoS₂@CCF loading range of 10 wt%-15 wt%, and then a sharp increase in ϵ' and ϵ'' from 6.7 to 13.6 and 3.0 to 9.0 is observed in the filler loading range of 15 wt%-25 wt%. After that, the growth rate of them slows down again from the 25 wt% WS₂/CoS₂@CCF loading. Hence, it can be induced that the filler loading range of 15 wt%-25 wt% is the percolation region, which is closely related with the filler loading dependent EMW absorption performance.

Based on the percolation theory, the corresponding mechanism is illustrated in [Figure 7c](#). The

dispersed low-content WS₂/CoS₂@CCF are isolated by paraffin where the interface between them can serve as micro-capacitor to store electric charge (Figure 7c-i). Meanwhile, the accumulated unbalanced charge at the interfaces can also result in the interfacial polarization loss under alternating electric field, which is a main attenuation mode towards the incident EMW. With the further increase in WS₂/CoS₂@CCF loading, more heterojunction interfaces are produced, both the electrical energy storage and interfacial polarization loss capability are significantly enhanced. Besides, partial WS₂/CoS₂@CCF also turns to be connected with each other to construct the local microcircuit, generating the additional conduction loss which is beneficial for improved EMW absorption performances (Figure 7c-ii). When the WS₂/CoS₂@CCF loading exceed a certain content (percolation threshold), stable conductive network is constructed, and the increase in conduction loss slows down. This can also be verified by the Cole–Cole curves in Figure 7d that the paraffin composites with 20 wt% WS₂/CoS₂@CCF possesses the most semicircles, but a longer linear tail is observed for the composites with higher loading, indicating the improved conductivity, which is coincided with the result shown in Figure 7e. However, excessive WS₂/CoS₂@CCF loading means stable conductive network and much higher conductivity (Figure 7c-iii), which will undoubtedly lead to poor impedance matching and reduced EMW absorption capacity. As a result, a 20 wt% filler loading is the most optimal value to achieve the strongest EMW absorption.

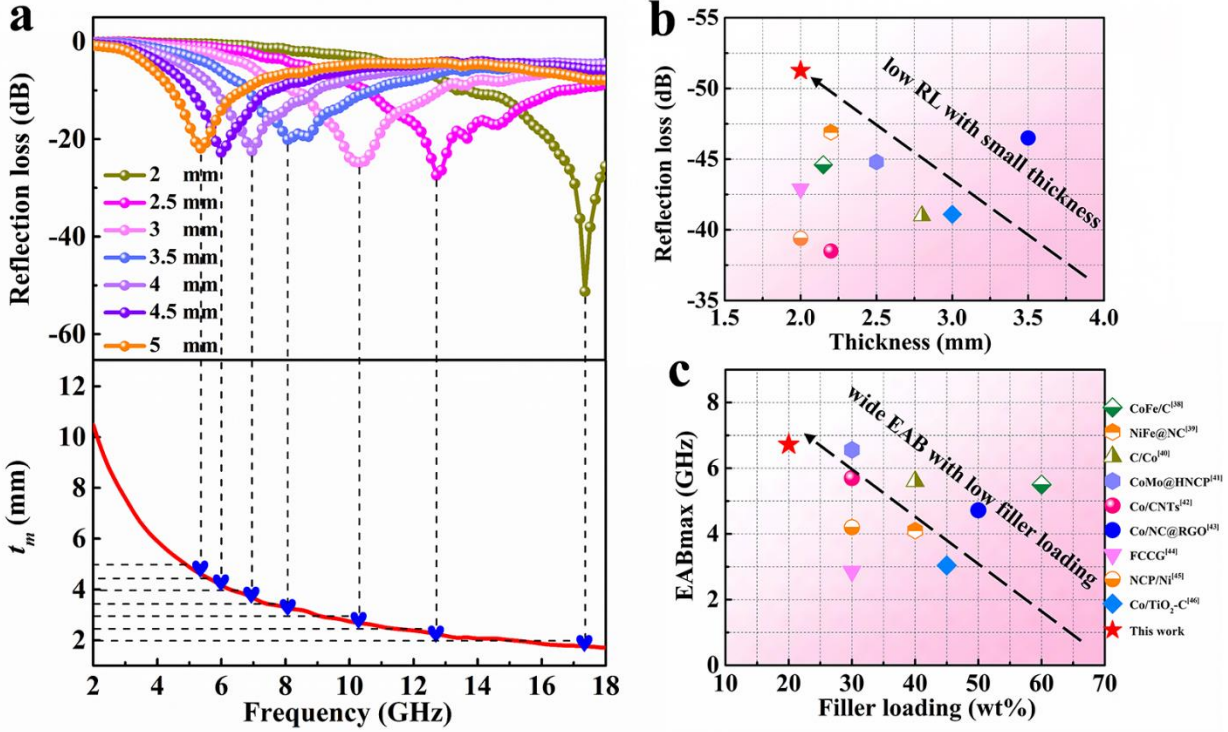


Figure 8. (a) The plots of RL values and quarter-wavelength matching model of WS₂/CoS₂@CCF with different thicknesses. Comparison of the EMW absorption performance of our prepared WS₂/CoS₂@CCF with other reported works: (b) RL versus matching thicknesses and (c) EAB versus filler contents.

Remarkably, the absorption peaks shifted to low frequency with increasing sample thickness from 2 to 5 mm, which can be explained by the 1/4 quarter wavelength cancellation formula: [36, 37]

$$t_m = n\lambda/4 = nc / \left(4f_m \sqrt{|\mu_r| |\varepsilon_r|} \right) (n = 1, 3, 5 \dots) \quad (7)$$

where t_m and f_m correspond to the matching thickness and matching frequency, respectively. When t_m and f_m conform to the equation, the incident and reflected wave at the interface of air and absorber are out of phase by 180°, enabling the total cancellation of reflected EMW and best EMW absorption capacity. As shown in Figure 8a, the blue heart symbols that correspond to the matching thickness of WS₂/CoS₂@CCF under 20 wt% filler loading are well coincided with simulated red line, indicating the EMW absorption capability of our prepared hierarchical heterostructure

WS₂/CoS₂@CCF conform to the quarter-wavelength cancellation model which endows it with the best EMW absorption performances. Furthermore, EMW absorption performances of our prepared hierarchical heterostructure WS₂/CoS₂@CCF were compared with other reported carbon-based magnetic-dielectric absorbers [38-46]. As displayed in Figure 8b&c, WS₂/CoS₂@CCF exhibits a strong absorption (-51.26 dB) at a thickness of only 2 mm and wide EAB (6.72 GHz) at low filler loading (20 wt%), which are superior to other absorbers. Generally, smaller matching thickness and lower filler loading imply a reduction of weight, which is just needed for the practical application. Thus, it can be claimed that the WS₂/CoS₂@CCF has great application potential for high-efficient EMW absorption.

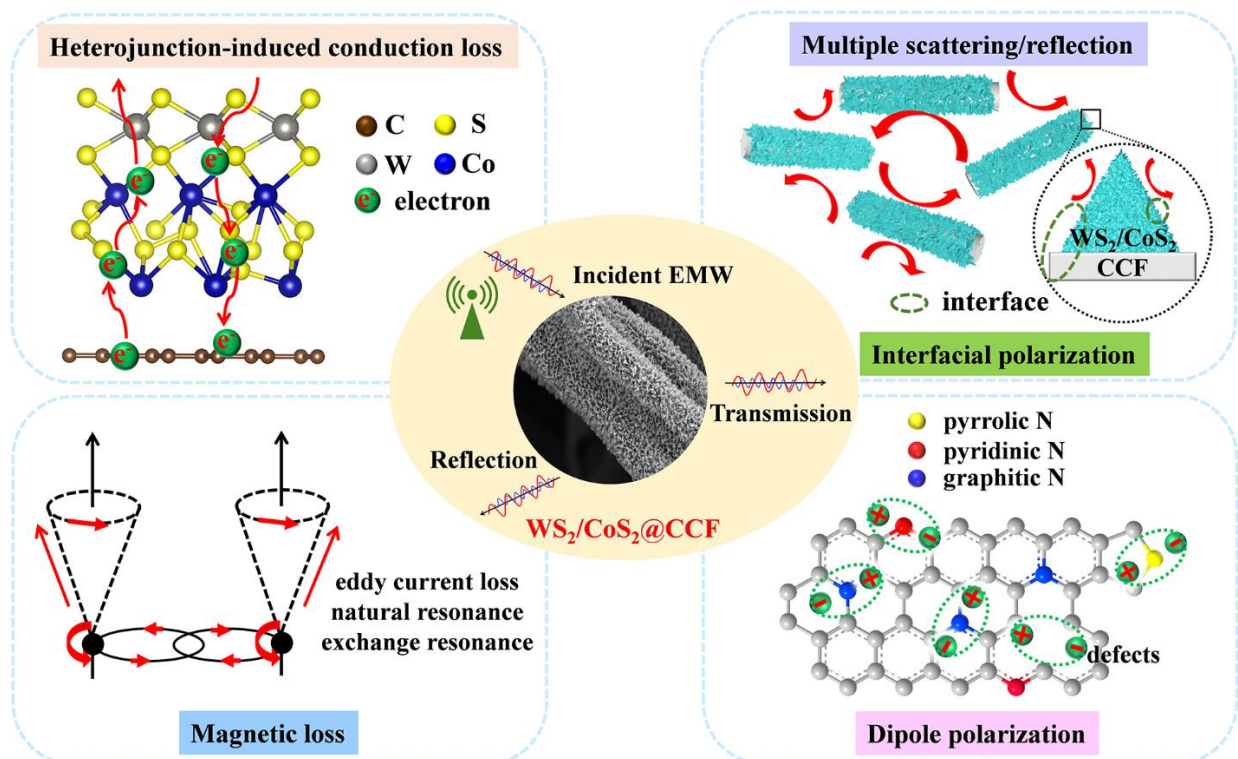


Figure 9. Schematic illustration of the microwave absorption mechanism for WS₂/CoS₂@CCF.

Based on the above analysis, the EMW absorption mechanism of WS₂/CoS₂@CCF is displayed

in Figure 9. Firstly, the low-electronegativity sulfur in heterogeneous WS_2/CoS_2 can effectively accelerate the transfer of electrons in the hierarchical heterostructure $\text{WS}_2/\text{CoS}_2@\text{CCF}$, generating significant heterojunction-induced conduction loss through the connected 3D conductive network. Secondly, the unique hierarchical porous structure is conducive to optimize the impedance matching and facilitate multiple scattering and reflection of incident microwave, further enhancing the attenuation capacity. Meanwhile, amounts of heterogenous interfaces of WS_2/CoS_2 and contact interfaces of $\text{WS}_2/\text{CoS}_2\text{-CCF}$ and $\text{WS}_2/\text{CoS}_2@\text{CCF}$ -paraffin can also induce powerful interface polarization loss. Furthermore, the residual functional groups, defects, and doped N and S elements in $\text{WS}_2/\text{CoS}_2@\text{CCF}$ act as active centers to promote the formation of dipoles under alternating electromagnetic field, generating the dipole polarization loss. Finally, the presence of magnetic WS_2/CoS_2 nanoflakes can also endow the hierarchical heterostructure material with suitable magnetic loss performance, such as exchange resonance, eddy current loss and natural resonance, which can further enhance the dissipation of EMW energy due to the synergistic effect of magnetic and dielectric loss. As a result, the multiple loss mechanisms make the hierarchical heterostructure $\text{WS}_2/\text{CoS}_2@\text{CCF}$ composite with excellent EMW absorption performance, thus providing a new route for the accurate design of advanced EMW absorbers.

4 Conclusions

To sum up, we designed a hierarchical heterostructure $\text{WS}_2/\text{CoS}_2@\text{CCF}$ with outstanding EMW performance, which was successfully prepared by using biomass resources and ZIF-67 as precursors through a facile and controllable etching, sulfurization, and carbonization approach. As

a result, the prepared WS₂/CoS₂@CCF shows a prominent RL_{min} of -51.26 dB with a thickness of 2 mm and a wider EAB of 6.72 GHz (11.28-18 GHz) when the filler loading is 20 wt%. The coexistence of magnetic and dielectric loss, special heterostructure and multicomponent are conducive to optimizing impedance matching. Moreover, the amounts of heterogenous WS₂/CoS₂ are also advantageous to increase dipole/interfacial polarization loss and conduction loss, generating improved EMW attenuation capability. Overall, this work offers a low-cost and novel method for designing hierarchical heterostructure materials for high-performance EMW absorbers.

Acknowledgements

This work was supported by National Natural Science Foundation of China (NO: 51803191, 12072325), National Key R&D Program of China (2019YFA0706802), the 111 project (D18023), Key Scientific and Technological Project of Henan Province (202102210038), and the Deanship of Scientific Research at Umm Al-Qura University (22UQU4331100DSR01).

Electronic Supplementary Material: Supplementary material (Digital photographs, SEM images, EDS pattern, XPS spectra, Cole-Cole curves, permeability parameters, reflection loss) is available in the online version of this article.

References

- [1] Lu, X.; Zhu, D.; Li, X.; Li, M.; Chen, Q.; Qing, Y. Gelatin-derived N-doped hybrid carbon nanospheres with an adjustable porous structure for enhanced electromagnetic wave absorption. *Adv Compos Hybrid Mater* **2021**, *4*, 946-956.
- [2] Zhang, Y.; Gu, J. A Perspective for Developing Polymer-Based Electromagnetic Interference Shielding Composites. *Nanomicro Lett* **2022**, *14*, 89.
- [3] Gao, Q.; Pan, Y.; Zheng, G.; Liu, C.; Shen, C.; Liu, X. Flexible multilayered MXene/thermoplastic polyurethane films with excellent electromagnetic interference shielding, thermal conductivity, and management performances. *Adv Compos Hybrid Mater* **2021**, *4*, 274-285.

- [4] Wu, N.; Du, W.; Hu, Q.; Vupputuri, S.; Jiang, Q. Recent Development in Fabrication of Co Nanostructures and Their Carbon Nanocomposites for Electromagnetic Wave Absorption. *Eng. Sci.* **2021**, *13*, 11-23.
- [5] Zhang, Y.; Ma, Z.; Ruan, K.; Gu, J. Multifunctional $\text{Ti}_3\text{C}_2\text{T}_x$ -(Fe_3O_4 /polyimide) composite films with Janus structure for outstanding electromagnetic interference shielding and superior visual thermal management. *Nano Res.* **2022**, 10.1007/s12274-022-4358-7.
- [6] Han, Y.; Ruan, K.; Gu, J. Janus (BNNS/ANF)-(AgNWs/ANF) thermal conductivity composite films with superior electromagnetic interference shielding and Joule heating performances. *Nano Res.* **2022**, 10.1007/s12274-022-4159-z.
- [7] Wang, Y.; Wang, P.; Du, Z.; Liu, C.; Shen, C.; Wang, Y. Electromagnetic interference shielding enhancement of poly (lactic acid)-based carbonaceous nanocomposites by poly (ethylene oxide)-assisted segregated structure: a comparative study of carbon nanotubes and graphene nanoplatelets. *Adv Compos Hybrid Mater* **2022**, *5*, 209-219.
- [8] Wang, L.; Ma, Z.; Zhang, Y.; Chen, L.; Cao, D.; Gu, J. Polymer-based EMI shielding composites with 3D conductive networks: A mini-review. *SusMat.* **2021**, *1*, 413-431.
- [9] Song, P.; Ma, Z.; Qiu, H.; Ru, Y.; Gu, J. High-Efficiency Electromagnetic Interference Shielding of rGO@FeNi/Epoxy Composites with Regular Honeycomb Structures. *Nanomicro Lett* **2022**, *14*, 51.
- [10] Zhu, X.; Qiu, H.; Chen, P.; Chen, G.; Min, W. Graphitic carbon nitride ($\text{g-C}_3\text{N}_4$) in situ polymerization to synthesize MOF-Co@CNTs as efficient electromagnetic microwave absorption materials. *Carbon* **2021**, *176*, 530-539.
- [11] Wang, Y.; Di, X.; Lu, Z.; Cheng, R.; Wu, X.; Gao, P. Controllable heterogeneous interfaces of cobalt/carbon nanosheets/rGO composite derived from metal-organic frameworks for high-efficiency microwave attenuation. *Carbon* **2022**, *187*, 404-414.
- [12] Guo, Y.; Wang, D.; Tian, Y.; Wang, J.; Bai, T.; Liu, H.; Guo, Z.; Liu, C.; Shen, C. FeCo alloy nanoparticle decorated cellulose based carbon aerogel as a low-cost and efficient electromagnetic microwave absorber. *J. Mater. Chem. C* **2022**, *10*, 126-134.
- [13] Cui, J.; Wang, X.; Huang, L.; Zhang, C.; Yuan, Y.; Li, Y. Environmentally friendly bark-derived Co-Doped porous carbon composites for microwave absorption. *Carbon* **2022**, *187*, 115-125.
- [14] Zhu, M.; Yan, X.; Xu, H.; Xu, Y.; Kong, L. Ultralight, compressible, and anisotropic MXene@Wood nanocomposite aerogel with excellent electromagnetic wave shielding and absorbing properties at different directions. *Carbon* **2021**, *182*, 806-814.
- [15] Zhang, X.; Dong, Y.; Pan, F.; Xiang, Z.; Zhu, X.; Lu, W. Electrostatic self-assembly construction of 2D MoS_2 wrapped hollow Fe_3O_4 nanoflowers@1D carbon tube hybrids for self-cleaning high-performance microwave absorbers. *Carbon* **2021**, *177*, 332-343.
- [16] Pan, F.; Liu, Z.; Deng, B.; Dong, Y.; Zhu, X.; Huang, C.; Lu, W. Lotus Leaf-Derived Gradient Hierarchical Porous C/ MoS_2 Morphology Genetic Composites with Wideband and Tunable Electromagnetic Absorption Performance. *Nanomicro Lett* **2021**, *13*, 43.
- [17] Wang, B.; Li, S.; Huang, F.; Wang, S.; Zhang, H.; Liu, F.; Liu, Q. Construction of multiple electron transfer paths in 1D core-shell heterostructures with MXene as interlayer enabling efficient microwave absorption. *Carbon* **2022**, *187*, 56-66.
- [18] Xu, X.; Ran, F.; Fan, Z.; Cheng, Z.; Xie, Z.; Lv, T.; Liu, Y. Microstructural engineering of flexible and broadband microwave absorption films with hierarchical superstructures derived from bimetallic metal-

- organic framework. *Carbon* **2021**, *178*, 320-331.
- [19] Zhang, D.; Wang, H.; Cheng, J.; Han, C.; Yang, X.; Xu, J.; Shan, G.; Zheng, G.; Cao, M. Conductive WS₂-NS/CNTs hybrids based 3D ultra-thin mesh electromagnetic wave absorbers with excellent absorption performance. *Appl. Surf. Sci.* **2020**, *528*, 147052.
- [20] Wu, J.; Chen, Tian.; Zhu, C.; Du, J.; Huang, L.; Yan, J.; Cai, D.; Guan, C.; Pan, C. Rational Construction of WS₂/CoS₂ Heterostructure Electrocatalyst for Efficient Hydrogen Evolution at All pH Values. *ACS Sustainable Chem. Eng.* **2020**, *8*, 4474-4480.
- [21] Guo, Y.; Wang, D.; Wang, J.; Tian, Y.; Liu, H.; Liu, C.; Shen, C. Hierarchical HCF@NC/Co Derived from Hollow Loofah Fiber Anchored with Metal-Organic Frameworks for Highly Efficient Microwave Absorption. *ACS Appl. Mater. Interfaces* **2022**, *14*, 2038-2050.
- [22] Ren, C.; Jia, X.; Zhang, W.; Hou, D.; Xia, Z.; Huang, D.; Hu, J.; Chen, S.; Gao, S. Hierarchical Porous Integrated Co_{1-x}S/CoFe₂O₄@rGO Nanoflowers Fabricated via Temperature-Controlled In Situ Calcining Sulfurization of Multivariate CoFe-MOF-74@rGO for High-Performance Supercapacitor. *Adv. Funct. Mater.* **2020**, *30*, 2004519.
- [23] Zhou, X.; Yang, X.; Li, H.; Hedhili, M. N.; Huang, K.-W.; Li, L.-J.; Zhang, W. Symmetric synergy of hybrid CoS₂-WS₂ electrocatalysts for the hydrogen evolution reaction. *J. Mater. Chem. A* **2017**, *5*, 15552-15558.
- [24] Ma, Z.; Xiang, X.; Shao, L.; Zhang, Y.; Gu, J. Multifunctional Wearable Silver Nanowire Decorated Leather Nanocomposites for Joule Heating, Electromagnetic Interference Shielding and Piezoresistive Sensing. *Angew. Chem. Int. Ed.* **2022**, *61*, e202200705.
- [25] Liu, P.; Zhu, C.; Gao, S.; Guan, C.; Huang, Y.; He, W. N-doped porous carbon nanoplates embedded with CoS₂ vertically anchored on carbon cloths for flexible and ultrahigh microwave absorption. *Carbon* **2020**, *163*, 348-359.
- [26] Wu, F.; Liu, Z.; Wang, J.; Shah, T.; Liu, P.; Zhang, Q.; Zhang, B. Template-free self-assembly of MXene and CoNi-bimetal MOF into intertwined one-dimensional heterostructure and its microwave absorbing properties. *Chem. Eng. J.* **2021**, *422*, 130591.
- [27] Sun, L.; Shi, Z.; He, B.; Wang, H.; Liu, S.; Huang, M.; Shi, J.; Dastan, D.; Wang, H. Asymmetric Trilayer All-Polymer Dielectric Composites with Simultaneous High Efficiency and High Energy Density: A Novel Design Targeting Advanced Energy Storage Capacitors. *Adv. Funct. Mater.* **2021**, *31*, 2100280.
- [28] Sun, S.; Shi, Z.; Sun, L.; Liang, L.; Dastan, D.; He, B.; Wang, H.; Huang, M.; Fan, R. Achieving Concurrent High Energy Density and Efficiency in All Polymer Layered Paraelectric/Ferroelectric Composites via Introducing a Moderate Layer. *ACS Appl. Mater. Interfaces* **2021**, *13*, 27522-27532.
- [29] Wang, Z.; Yang, L.; Zhou, Y.; Xu, C.; Yan, M.; Wu, C. NiFe LDH/MXene Derivatives Interconnected with Carbon Fabric for Flexible Electromagnetic Wave Absorption. *ACS Appl. Mater. Interfaces* **2021**, *13*, 16713-16721.
- [30] Wang, Y.; Zhong, W.; Zhang, S.; Zhang, X.; Zhu, C.; Zhang, X.; Zhang, X.; Chen, Y. Pearl necklace-like CoMn-based nanostructures derived from metal-organic frames for enhanced electromagnetic wave absorption. *Carbon* **2022**, *188*, 254-264.
- [31] Song, S.; Zhang, A.; Chen, L.; Jia, Q.; Zhou, C.; Liu, J.; Wang, X. A novel multi-cavity structured MOF derivative/porous graphene hybrid for high performance microwave absorption. *Carbon* **2021**, *176*, 279-289.
- [32] Tan, R.; Zhou, J.; Yao, Z.; Wei, B.; Zu, J.; Lin, H.; Li, Z. Ferrero Rocher[®] chocolates-like FeCo/C microspheres with adjustable electromagnetic properties for effective microwave absorption. *J. Alloys Compd.*

- 2021**, 857, 157568.
- [33] Guo, Y.; Wang, D.; Bai, T.; Liu, H.; Zheng, Y.; Liu, C.; Shen, C. Electrostatic self-assembled NiFe₂O₄/Ti₃C₂T_x MXene nanocomposites for efficient electromagnetic wave absorption at ultralow loading level. *Adv Compos Hybrid Mater* **2021**, 4, 602-613.
- [34] Wei, H.; Tian, Y.; Chen, Q.; Estevez, D.; Xu, P.; Peng, H.-X.; Qin, F. Microwave absorption performance of 2D Iron-Quinoid MOF. *Chem. Eng. J.* **2021**, 405, 126637.
- [35] Zhao, B.; Deng, J.; Zhang, R.; Liang, L.; Fan, B.; Bai, Z.; Shao, G.; Park, C. B. Recent Advances on the Electromagnetic Wave Absorption Properties of Ni Based Materials. *Eng. Sci.* **2018**, 3, 5-40.
- [36] Li, X.; Wang, Z.; Xiang, Z.; Zhu, X.; Dong, Y.; Huang, C.; Cai, L.; Lu, W. Biconical prisms Ni@C composites derived from metal-organic frameworks with an enhanced electromagnetic wave absorption. *Carbon* **2021**, 184, 115-126.
- [37] Bai, T.; Guo, Y.; Liu, H.; Song, G.; Zhang, D.; Wang, Y.; Mi, L.; Guo, Z.; Liu, C.; Shen, C. Achieving enhanced electromagnetic shielding and absorption capacity of cellulose-derived carbon aerogels via tuning the carbonization temperature. *J. Mater. Chem. C* **2020**, 8, 5191-5201.
- [38] Liang, X.; Wang, G.; Gu, W.; Ji, G. Prussian blue analogue derived carbon-based composites toward lightweight microwave absorption. *Carbon* **2021**, 177, 97-106.
- [39] Qu, X.; Zhou, Y.; Li, X.; Javid, M.; Huang, F.; Zhang, X.; Dong, X.; Zhang, Z. Nitrogen-doped graphene layer-encapsulated NiFe bimetallic nanoparticles synthesized by an arc discharge method for a highly efficient microwave absorber. *Inorg. Chem. Front.* **2020**, 7, 1148-1160.
- [40] Peng, C.; Zhang, Y.; Zhang, B. MOF-derived jujube pit shaped C/Co composites with hierarchical structure for electromagnetic absorption. *J. Alloys Compd.* **2020**, 826, 154203.
- [41] Huang, W.; Zhang, X.; Zhao, Y.; Zhang, J.; Liu, P. Hollow N-doped carbon polyhedra embedded Co and Mo₂C nanoparticles for high-efficiency and wideband microwave absorption. *Carbon* **2020**, 167, 19-30.
- [42] Yan, J.; Huang, Y.; Zhang, Z.; Liu, X. Novel 3D microsheets contain cobalt particles and numerous interlaced carbon nanotubes for high-performance electromagnetic wave absorption. *J. Alloys Compd.* **2019**, 785, 1206-1214.
- [43] Liu, L.; Wang, L.; Li, Q.; Yu, X.; Shi, X.; Ding, J.; You, W.; Yang, L.; Zhang, Y.; Che, R. High-Performance Microwave Absorption of MOF-Derived Core-Shell Co@N-doped Carbon Anchored on Reduced Graphene Oxide. *ChemNanoMat* **2019**, 5, 558-565.
- [44] Li, N.; Huang, G.; Xiao, H.; Feng, Q.; Fu, S. Investigations on structure-dependent microwave absorption performance of nano-Fe₃O₄ coated carbon-based absorbers. *Carbon* **2019**, 144, 216-227.
- [45] Quan, B.; Xu, G.; Yi, H.; Yang, Z.; Xiang, J.; Chen, Y.; Ji, G. Enhanced electromagnetic wave response of nickel nanoparticles encapsulated in nanoporous carbon. *J. Alloys Compd.* **2018**, 769, 961-968.
- [46] Liao, Q.; He, M.; Zhou, Y.; Nie, S.; Wang, Y.; Wang, B.; Yang, X.; Bu, X.; Wang, R. Rational Construction of Ti₃C₂T_x/Co-MOF-Derived Laminated Co/TiO₂-C Hybrids for Enhanced Electromagnetic Wave Absorption. *Langmuir* **2018**, 34, 15854-15863.